Effects of Metal Ions on Physicochemical Properties and Redox Reactivity of Phenolates and Phenoxyl Radicals: Mechanistic Insight into Hydrogen Atom Abstraction by Phenoxyl Radical−Metal Complexes

Shinobu Itoh,*,† Hideyuki Kumei,‡ Shigenori Nagatomo,§ Teizo Kitagawa,*,§ and Shunichi Fukuzumi*,‡

Contribution from the Department of Chemistry, Graduate School of Science, Osaka City University, 3-3-138 Sugimoto, Sumiyoshi-ku, Osaka 558-8585, Japan, Department of Material and Life Science, Graduate School of Engineering, Osaka University, CREST, Japan Science and Technology Corporation, 2-1 Yamada-oka, Suita, Osaka 565-0871, Japan, and Institute for Molecular Science, Myodaiji, Okazaki 444-8585, Japan

Received October 6, 2000

Abstract: Phenolate and phenoxyl radical complexes of a series of alkaline earth metal ions as well as monovalent cations such as Na^+ and K^+ have been prepared by using 2,4-di-*tert*-butyl-6-(1,4,7,10-tetraoxa-13-aza-cyclopentadec-13-ylmethyl)phenol (**L1H**) and 2,4-di-*tert*-butyl-6-(1,4,7,10,13-pentaoxa-16-aza-cyclooctadec-16-ylmethyl)phenol (**L2H**) to examine the effects of the cations on the structure, physicochemical properties and redox reactivity of the phenolate and phenoxyl radical complexes. Crystal structures of the Mg^{2+}- and Ca^{2+}-complexes of $\mathbf{L1}^-$ as well as the Ca^{2+}- and Sr^{2+}-complexes of $\mathbf{L2}^-$ were determined by X-ray crystallographic analysis, showing that the crown ether rings in the Ca^{2+}-complexes are significantly distorted from planarity, whereas those in the Mg^{2+}- and Sr^{2+}-complexes are fairly flat. The spectral features (UV−vis) as well as the redox potentials of the phenolate complexes are also influenced by the metal ions, depending on the Lewis acidity of the metal ions. The phenoxyl radical complexes are successfully generated in situ by the oxidation of the phenolate complexes with $(NH_4)_2[Ce^{4+}(NO_3)_6]$ (CAN). They exhibited strong absorption bands around 400 nm together with a broad one around 600−900 nm, the latter of which is also affected by the metal ions. The phenoxyl radical−metal complexes are characterized by resonance Raman, ESI-MS, and ESR spectra, and the metal ion effects on those spectroscopic features are also discussed. Stability and reactivity of the phenoxyl radical−metal complexes are significantly different, depending on the type of metal ions. The disproportionation of the phenoxyl radicals is significantly retarded by the electronic repulsion between the metal cation and a generated organic cation ($\mathbf{Ln}^+$), leading to stabilization of the radicals. On the other hand, divalent cations decelerate the rate of hydrogen atom abstraction from 10-methyl-9,10-dihydroacridine ($AcrH_2$) and its 9-substituted derivatives (AcrHR) by the phenoxyl radicals. On the basis of primary kinetic deuterium isotope effects and energetic consideration of the electron-transfer step from $AcrH_2$ to the phenoxyl radical−metal complexes, we propose that the hydrogen atom abstraction by the phenoxyl radical−alkaline earth metal complexes proceeds via electron transfer followed by proton transfer.

Introduction

Protein radicals are now well recognized to play a crucial role in several biologically important redox processes.[1] In particular, organic radicals derived from tyrosine and its derivatives have been reported to participate in a variety of enzymatic catalysis such as in class I ribonucleotide reductase (RNR), photosystem II, prostaglandin H synthase, galactose oxidase, cytochrome *c* oxidase, bovine liver catalase, DNA photolyase, and so on.[1−6] In these cases, the tyrosine radical mainly acts as a hydrogen atom acceptor to induce C−H bond activation of the substrate, which is the initial step of the above enzymatic reactions.[1] Transition-metal ions bound to a tyrosine radical have also been proven to enhance the radical stability as well as to control reactivity of the phenoxyl radical species. One of the most well-documented examples of such systems is galactose oxidase,[7] where a tyrosine radical coordinated to copper(II) acts as an active species for the oxidation of primary alcohols to the corresponding aldehydes.[8] Extensive efforts have so far been made not only to mimic the biochemical reactivity of galactose oxidase but also to provide valuable insight into

† Department of Chemistry, Graduate School of Science, Osaka City University.

‡ Department of Material and Life Science, Graduate School of Engineering, Osaka University.

§ Institute for Molecular Science.

(1) Stubbe, J.; van der Donk, W. A. *Chem. Rev.* **1998**, *98*, 705−762 and references therein.

(2) Babcock, G. T.; Espe, M.; Hoganson, C.; Lydakis-Simantiris, N.; McCracken, J.; Shi, W.; Styring, S.; Tommos, C.; Warncke, K. *Acta Chem. Scand.* **1997**, *51*, 533−540.

(3) Gerfen, G. J.; Bellew, B. F.; Griffin, R. G.; Singel, D. J.; Ekberg, C. A.; Whittaker, J. W. *J. Phys. Chem.* **1996**, *100*, 16739−16748.

(4) MacMillan, F.; Kannt, A.; Behr, J.; Prisner, T.; Michel, H. *Biochemistry* **1999**, *38*, 9179−9184.

(5) Ivancich, A.; Jouve, H. M.; Gaillard, J. *J. Am. Chem. Soc.* **1996**, *118*, 12852−12853.

(6) Aubert, C.; Brettel, K.; Mathis, P.; Eker, A. P. M.; Boussac, A. *J. Am. Chem. Soc.* **1999**, *121*, 8659−8660.

(7) Ito, N.; Phillips, S. E. V.; Stevens, C.; Ogel, Z. B.; McPherson, M. J.; Keen, J. N.; Yadav, K. D. S.; Knowles, P. F. *Nature* **1991**, *350*, 87−90.

10.1021/ja0036110 CCC: $20.00
Published on Web 02/14/2001

the general aspects of structures, physicochemical properties, and functions of phenoxyl radical complexes with a series of transition-metal ions.[9−16]

The essential roles of metal ions have also been well recognized in a variety of enzymatic functions.[17−19] A number of attempts are being made not only to detect but also to chemically and functionally characterize trace elements or otherwise inconspicuous metal ions in various enzymes. The catalytic role of alkaline earth metal ions in enzymatic redox reactions has particularly merited recent attention, since a growing number of redox enzymes have been demonstrated to involve Ca^{2+} at their active sites, where Ca^{2+} is located near the redox cofactor.[20−24] Although very little is known about the catalytic roles of Ca^{2+} in such systems, one can assume that the interaction of the redox cofactor with the cationic species results in enhancement of the oxidation ability of the enzymes. In this context, we have recently demonstrated that the oxidation of primary alkyl alcohols is made possible by coenzyme PQQ (pyrroloquinolinequinone) of quinoprotein alcohol and glucose dehydrogenases,[23,24] when it coordinates to Ca^{2+} in the model system.[25,26] It has been shown that Ca^{2+} enhances electrophilicity of the quinone and stability of the reaction intermediates.[26] However, little is known about the effects of alkaline earth metal ions on the redox reactivity of organic radicals.

In this study, we have systematically investigated the effects of cationic species such as alkaline metal and alkaline earth metal ions on the structures, physicochemical properties, and redox reactivity of phenolate and phenoxyl radical species by using phenol derivatives **L1H** and **L2H** containing 1-aza-15-crown-5-ether and 1-aza-18-crown-6-ether group as the metal ion binding site, respectively.[27,28] It is shown that the stability of phenoxyl radical species is greatly enhanced by the interaction with the divalent metal ions, particularly with Ca^{2+}. The effects of metal ions on the oxidation ability of phenoxyl radicals are also examined by using 10-methyl-9,10-dihydroacridine ($AcrH_2$) and its 9-substituted derivatives (AcrHR) as substrates, providing valuable mechanistic insight into the C−H bond activation by the phenoxyl radical−metal complexes. This study will eventually stimulate the use of radical−metal complexes also in nonbiological redox reactions such as metal ion-catalyzed electron-transfer reactions of organic radicals.[29]

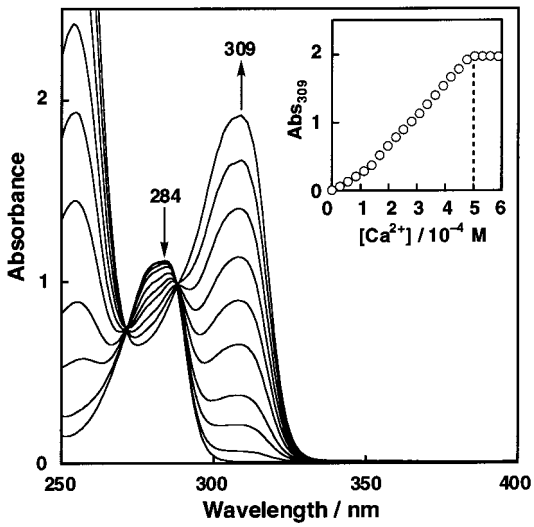

Figure 1. Spectral change observed upon addition of $Ca(ClO_4)_2 \cdot 4H_2O$ into a CH_3CN solution of **L1H** (5.0×10^{-4} M) in the presence of Et_3N (5.0×10^{-4} M), Inset: plot of the absorbance change at 309 nm against the concentration of Ca^{2+} added.

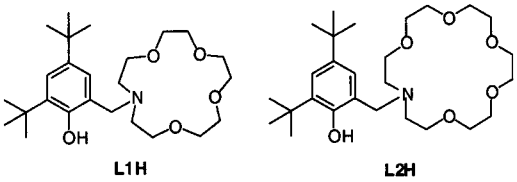

Results and Discussion

Synthesis and Characterization of Phenolate−Metal Complexes. The phenol derivatives containing 1-aza-15-crown-5-ether (**L1H**) and 1-aza-18-crown-6-ether group (**L2H**) have been prepared by Mannich reaction on 2,4-di-*tert*-butylphenol with the corresponding aza crown ether and paraformaldehyde in refluxing ethanol. Ligands **L1H** and **L2H** exhibit an absorption band at 284 and 283 nm in CH_3CN, respectively, which shifted toward the longer-wavelength region when an alkaline earth metal ion was added into the solution containing the ligand and triethylamine as a base. Such a red-shift of the absorption band is indicative of formation of the phenolate derivatives. A typical example of the titration of **L1H** with Ca^{2+} is shown in Figure 1, where the absorption band at 309 nm due to the Ca^{2+}-complex

(8) Whittaker, M. M.; Ballou, D. P.; Whittaker, J. W. *Biochemistry* **1998**, *37*, 8426−8436, and references therein.
(9) Itoh, S.; Taki, M.; Fukuzumi, S. *Coord. Chem. Rev.* **2000**, *198*, 3−20, and references therein.
(10) Halfen, J. A.; Jazdzewski, B. A.; Mahapatra, S.; Berreau, L. M.; Wilkinson, E. C.; Que, L., Jr.; Tolman, W. B. *J. Am. Chem. Soc.* **1997**, *119*, 8217−8227.
(11) Wang, Y.; Stack, T. D. P. *J. Am. Chem. Soc.* **1996**, *118*, 13097−13098.
(12) Hockertz, J.; Steenken, S.; Wieghardt, K.; Hildebrandt, P. *J. Am. Chem. Soc.* **1993**, *115*, 11222−11230.
(13) Sokolowski, A.; Bothe, E.; Bill, E.; Weyhermüller, T.; Wieghardt, K. *Chem. Commun.* **1996**, 1671−1672.
(14) Adam, B.; Bill, E.; Bothe, E.; Goerdt, B.; Haselhorst, G.; Hildenbrand, K.; Sokolowski, A.; Steenken, S.; Weyhermüller, T.; Wieghardt, K. *Chem. Eur. J.* **1997**, *3*, 308−319.
(15) Sokolowski, A.; Müller, J.; Weyhermüller, T.; Schnepf, R.; Hildebrandt, P.; Hildenbrand, K.; Bothe, E.; Wieghardt, K. *J. Am. Chem. Soc.* **1997**, *119*, 8889−8900.
(16) Sokolowski, A.; Adam, B.; Weyhermüller, T.; Kikuchi, A.; Hildenbrand, K.; Schnepf, R.; Hildebrandt, P.; Bill, E.; Wieghardt, K. *Inorg. Chem.* **1997**, *36*, 3702−3710.
(17) Hughes, M. N. *The Inorganic Chemistry of Biological Processes*, 2nd ed.; John Wiley & Sons: New York, 1984.
(18) Kaim, W. Schwederski, B. *Bioinorganic Chemistry: Inorganic Elements in the Chemistry of Life*; John Wiley & Sons: New York, 1994.
(19) Lippard, S. J.; Berg, J. M. *Principles of Bioinorganic Chemistry*; University Science Books: Mill Valley, California, 1994.
(20) Limburg, J.; Szalai, V. A.; Brudvig, G. W. *J. Chem. Soc., Dalton Trans.* **1999**, 1353−1361 and references therein.
(21) Einsle, O.; Messerschmidt, A.; Stach, P.; Bourenkov, G. P.; Bartunik, H. D.; Huber, R.; Kroneck, P. M. H. *Nature* **1999**, *400*, 476−480.
(22) Riistama, S.; Laakkonen, L.; Wikström, M.; Verkhovsky, M. I.; Puustinen, A. *Biochemistry* **1999**, *38*, 10670−10677.
(23) Xia, Z.-X.; Dai, W.-W.; Zhang, Y.-F.; White, S. A.; Boyd, G. D.; Mathews, F. S. *J. Mol. Biol.* **1996**, *259*, 480−501.
(24) Ghosh, M.; Anthony, C.; Harlos, K.; Goodwin, M. G.; Blake, C. *Structure* **1995**, *3*, 177−187.
(25) Itoh, S.; Kawakami, H.; Fukuzumi, S. *J. Am. Chem. Soc.* **1997**, *119*, 439−440.
(26) Itoh, S.; Kawakami, H.; Fukuzumi, S. *Biochemistry* **1998**, *37*, 6562−6571.
(27) To distinguish the different states of the phenol moiety of the ligands more clearly, the symbols of **LnH**, **Ln**$^-$, and **Ln**$^\bullet$ (**n** = **1** or **2**) are used to denote the phenol, phenolate, and phenoxyl radical forms, respectively.
(28) Modulation of redox properties of organic cofactors such as flavin by noncovalent weak interactions have been extensively studied by Rotello et al.; Niemz, A.; Rotello, V. M. *Acc. Chem. Res.* **1999**, *32*, 44−52 and references therein.
(29) (a) Fukuzumi, S. *Bull. Chem. Soc. Jpn.* **1997**, *70*, 1−28. (b) Fukuzumi, S. In *Advances in Electron-Transfer Chemistry*; Mariano, P. S., Ed.; JAI Press: Greenwich, CT, 1992; Vol. 2, pp. 67−175. (c) Fukuzumi, S.; Itoh, S. In *Advances in Photochemistry*; Neckers, D. C., Volman, D. H., von Bünau, G., Eds.; Wiley: New York, 1998; Vol. 25, pp 107−172. (d) Fukuzumi, S. In *Electron Transfer in Chemistry*; Balzani, V., Ed.; Wiley-VCH: Weinheim, 2000; Vol. 5 in press.

Table 1. Spectral Data of the Phenolate Complexes Generated in the Titration of **L1H** or **L2H** with $M(ClO_4)_2$ (M = Alkaline Earth Metal Ions) in the Presence of Triethylamine in CH_3CN[a,b]

	λ_{max}/nm (ϵ/M^{-1} cm^{-1})	
metal ion	**L1**$^-$	**L2**$^-$
Mg^{2+}	304 (4000)	301 (4400)
Ca^{2+}	309 (3940)	306 (4820)
Sr^{2+}	310 (4160)	308 (4840)
Ba^{2+}	311 (3460)	310 (3560)
Na^+ [a]	320 (5520)	−
K^+ [a]	−	312 (3100)[c]
$N(^nBu)_4^+$ [b]	317 (3740)	317 (4380)

[a] Since addition of $NaClO_4$ or $KClO_4$ into a CH_3CN solution of the phenol containing triethylamine resulted in little change of the UV−vis spectrum (see text), the Na^+-complex of **L1**$^-$ and the K^+-complex of **L2**$^-$were prepared by the reaction of the ligands (**L1H** and **L2H**) and the metal hydrides, NaH and KH, respectively (see Experimental Section). The spectral data are of the isolated products. [b] The tetra-*n*-butylammonium salts of the phenolate were generated in situ by adding tetra-*n*-butylammonium hydroxide $[N(^nBu)_4OH]$ to the phenol. [c] Because of low solubility of [K(**L2**$^-$)] in CH_3CN, the spectrum was taken in CH_3CN containing 10% CH_3OH.

increases with a concomitant decrease in the absorption band at 284 nm of **L1H** with clear isosbestic points at 271 and 288 nm. Since the spectral change is completed by the addition of just one equivalent of Ca^{2+} (see inset of Figure 1), a 1:1-complex between **L1**$^-$ and Ca^{2+} is formed effectively.[27] Spectral data for the titration of the ligands with a series of alkaline earth metal ions are summarized in Table 1. It should be noted that addition of $NaClO_4$ instead of divalent cations such as Ca^{2+} hardly affected the spectrum of the ligand under otherwise the same experimental conditions. This indicates that association of the monovalent cation and the phenol derivative is significantly small as compared to that with the divalent cations.

The λ_{max} values of the phenolate−metal complexes are blue-shifted in going from Na^+ to Mg^{2+}. The stronger Lewis acid such as Mg^{2+} may attract the negative charge of the phenolate oxygen more strongly than the weaker acids, making the transition energy of the $\pi-\pi^*$ of the phenolate ring higher. Molecular orbital calculations on the Mg^{2+}-complex of **L1**$^-$ by a ZINDO program could reproduce the UV−vis spectrum, where the calculated value of λ_{max} = 312 nm is comparable with the experimental value (λ_{max} = 304 nm in Table 1). This absorption band corresponds to the $\pi-\pi^*$ (HOMO-to-LUMO) transition.[30] The calculated $\pi-\pi^*$ transition energies of the Na^+-complex and the metal-free form of **L1**$^-$ are lower in energy and thereby the calculated λ_{max} values for both species are red-shifted (330 and 349 nm, respectively) as compared to that of the Mg^{2+}-complex of **L1**$^-$. The result of the MO calculation is consistent with the experimental observation shown in Table 1.[31]

The 1:1-complexes formed between **L1**$^-$ (and **L2**$^-$) and a series of alkaline earth metal ions were successfully isolated as BPh_4^- salts except for the Mg^{2+}-complex of **L2**$^-$. The structures of the Mg^{2+}- and Ca^{2+}-complexes of **L1**$^-$ as well as the Ca^{2+}- and Sr^{2+}-complexes of **L2**$^-$ were determined by X-ray crystallography. The crystallographic data and selected bond distances and angles for the X-ray structures are summarized in Tables 2 and 3. ORTEP drawings of the cationic parts of [Mg(**L1**$^-$)(CH_3OH)]BPh_4, [Ca(**L1**$^-$)(CH_3OH)$_2$]BPh_4, [Ca(**L2**$^-$)-(H_2O)]BPh_4, and [Sr(**L2**$^-$)(H_2O)]BPh_4 are shown in Figure 2a−d, respectively. As demonstrated by the UV−vis titration, each complex has one metal ion held in the crown ether cavity, which is also strongly associated with the phenolate oxygen. Each complex has additional external ligands such as CH_3OH in the Mg^{2+}- and Ca^{2+}-complexes of **L1**$^-$ and H_2O in the Ca^{2+}- and Sr^{2+}-complexes of **L2**$^-$, making the coordination number of the metal center seven or eight.

The Mg^{2+}-complex ([Mg(**L1**$^-$)(CH_3OH)]BPh_4) in Figure 2a has a nearly perfect pentagonal bipyramidal structure in which four oxygen atoms [O(2), O(3), O(4), and O(5)] and one tertiary amine nitrogen atom [N(1)] of the crown ether ring are placed in the pentagonal plane, and the phenolate and methanol oxygen atoms [O(1) and O(6)] coordinate to the metal ion in the opposite

Table 2. Summary of X-ray Crystallographic Data

compound	[Mg(**L1**$^-$)(CH_3OH)]BPh_4	[Ca(**L1**$^-$)(CH_3OH)$_2$]-BPh_4·2CH_3OH
empirical formula	$C_{50}H_{66}NO_6BMg$	$C_{53}H_{78}NO_9BCa$
formula weight	812.19	924.09
crystal system	triclinic	monoclinic
space group	$P\bar{1}$ (no. 2)	$C2/c$ (no. 15)
a, Å	13.2719(9)	35.486(2)
b, Å	15.321(1)	17.9443(9)
c, Å	12.3308(7)	17.8958(8)
α, deg	108.050(3)	
β, deg	94.392(2)	104.803(1)
γ, deg	99.524(2)	
V, Å^3	2329.1(3)	11017.3(9)
Z	2	8
F(000)	876.00	4000.00
D_{calc}, g/cm^3	1.158	1.114
T, °C	23	23
crystal size, mm	0.30 × 0.30 × 0.10	0.30 × 0.30 × 0.30
μ (Mo Kα), cm^{-1}	0.86	1.64
diffractometer	Rigaku RAXIS-RAPID Imaging Plate	Rigaku RAXIS-RAPID Imaging Plate
radiation	Mo Kα (0.71069 Å)	Mo Kα (0.71069 Å)
$2\theta_{max}$, deg	55.0	55.0
no. of reflns measd	20277	49660
no. of reflns obsd	9839 [$I > -10.00\sigma(I)$]	12570 [$I > -10.00\sigma(I)$]
no. of variables	784	814
R^a; R_w^b	0.183; 0.163	0.189; 0.180
R1[c]	0.076	0.076

compound	[Ca(**L2**$^-$)(H_2O)]BPh_4	[Sr(**L2**$^-$)(H_2O)]BPh_4
empirical formula	$C_{51}H_{68}NO_7BCa$	$C_{51}H_{68}NO_7BSr$
formula weight	857.99	905.53
crystal system	monoclinic	monoclonic
space group	$P2_1/n$ (no. 14)	$P2_1/n$ (no. 14)
a, Å	16.7447(6)	19.3828(9)
b, Å	18.4217(7)	17.9403(8)
c, Å	17.3976(5)	30.569(1)
β, deg	116.619(1)	107.3743(8)
V, Å^3	4797.7(3)	10153.8(8)
Z	4	8
F(000)	1848.00	3888.00
D_{calc}, g/cm^3	1.188	1.198
T, °C	23	23
crystal size, mm	0.30 × 0.30 × 0.10	0.25 × 0.25 × 0.10
μ (Mo Kα), cm^{-1}	1.81	11.09
diffractometer	Rigaku RAXIS-RAPID Imaging Plate	Rigaku RAXIS-RAPID Imaging Plate
radiation	Mo Kα (0.71069 Å)	Mo Kα (0.71069 Å)
$2\theta_{max}$, deg	55.0	55.0
no. of reflns measd	41971	21959
no. of reflns obsd	10775 [$I > 0.00\sigma(I)$]	5712 [$I > 2.00\sigma(I)$]
no. of variables	750	1108
R^a; R_w^b	0.162; 0.170	0.194; 0.248
R1[c]	0.065	0.113

[a] $R = \sum(F_o^2 - F_c^2)/\sum F_o^2$. [b] $R_w = (\sum\omega(F_o^2 - F_c^2)^2/\sum\omega(F_o^2))^{1/2}$; $\omega = 1/\sigma^2(F_o)$. [c] $R1 = \sum||F_o| - |F_c||/\sum|F_o|$.

(30) The ZINDO calculation was carried out on a Mg^{2+} complex of **L1**$^-$ containing one methanol molecule as an external ligand based on the X-ray structure of complex shown in Figure 2a.

(31) The general trend of λ_{max} depending on different metal ions can be well reproduced by the ZINDO calculations, although the calculated λ_{max} values are always a little larger than the experimental values.

Table 3. Selected Bond Lengths (Å) and Angles (deg)[a]

[Mg(**L1**$^-$)(CH$_3$OH)]BPh$_4$

Mg(1)−O(1)	1.957(2)	Mg(1)−O(2)	2.158(2)	Mg(1)−O(5)	2.207(2)	Mg(1)−O(6)	2.113(2)
Mg(1)−O(3)	2.236(2)	Mg(1)−O(4)	2.181(2)	Mg(1)−N(1)	2.290(2)		
O(1)−Mg(1)−O(2)	95.97(8)	O(1)−Mg(1)−−O(3)	94.07(7)	O(3)−Mg(1)−O(5)	140.42(8)	O(3)−Mg(1)−O(6)	86.41(8)
O(1)−Mg(1)−O(4)	91.32(8)	O(1)−Mg(1)−O(5)	101.07(8)	O(3)−Mg(1)−N(1)	143.25(8)	O(4)−Mg(1)−O(5)	71.89(8)
O(1)−Mg(1)−O(6)	177.73(9)	O(1)−Mg(1)−N(1)	88.50(7)	O(4)−Mg(1)−O(6)	86.73(9)	O(4)−Mg(1)−N(1)	145.26(9)
O(2)−Mg(1)−O(3)	70.42(8)	O(2)−Mg(1)−O(4)	141.53(9)	O(5)−Mg(1)−O(6)	77.23(8)	O(5)−Mg(1)−N(1)	74.08(8)
O(2)−Mg(1)−O(5)	142.15(9)	O(2)−Mg(1)−O(6)	86.28(9)	O(6)−Mg(1)−N(1)	92.44(8)	Mg(1)−O(1)−C(1)	126.1(2)
O(2)−Mg(1)−N(1)	72.85(8)	O(3)−Mg(1)−O(4)	71.41(8)				

[Ca(**L1**$^-$)(CH$_3$OH)$_2$]BPh$_4$·2CH$_3$OH

Ca(1)−O(1)	2.315(2)	Ca(1)−O(2)	2.513(2)	Ca(1)−O(5)	2.462(2)	Ca(1)−O(6)	2.444(3)
Ca(1)−O(3)	2.607(2)	Ca(1)−O(4)	2.554(2)	Ca(1)−O(7)	2.450(2)	Ca(1)−N(1)	2.623(3)
O(1)−Ca(1)−O(2)	140.22(7)	O(1)−Ca(1)−O(3)	153.41(8)	O(3)−Ca(1)−O(7)	92.36(8)	O(3)−Ca(1)−N(1)	128.68(8)
O(1)−Ca(1)−O(4)	104.72(7)	O(1)−Ca(1)−O(5)	90.28(7)	O(4)−Ca(1)−O(5)	65.40(7)	O(4)−Ca(1)−O(6)	75.94(7)
O(1)−Ca(1)−O(6)	79.80(7)	O(1)−Ca(1)−O(7)	85.81(7)	O(4)−Ca(1)−O(7)	145.10(8)	O(4)−Ca(1)−N(1)	131.41(8)
O(1)−Ca(1)−N(1)	77.49(7)	O(2)−Ca(1)−O(3)	63.42(7)	O(5)−Ca(1)−O(6)	136.08(8)	O(5)−Ca(1)−O(7)	149.00(8)
O(2)−Ca(1)−O(4)	111.11(7)	O(2)−Ca(1)−O(5)	89.30(7)	O(5)−Ca(1)−N(1)	66.07(7)	O(6)−Ca(1)−O(7)	73.35(8)
O(2)−Ca(1)−O(6)	124.88(8)	O(2)−Ca(1)−O(7)	74.74(7)	O(6)−Ca(1)−N(1)	148.24(8)	O(7)−Ca(1)−N(1)	83.09(9)
O(2)−Ca(1)−N(1)	66.12(7)	O(3)−Ca(1)−O(4)	63.37(7)	Ca(1)−O(1)−C(1)	131.7(2)		
O(3)−Ca(1)−O(5)	104.20(7)	O(3)−Ca(1)−O(6)	74.29(7)				

[Ca(**L2**$^-$)(H$_2$O)]BPh$_4$

Ca(1)−O(1)	2.245(2)	Ca(1)−O(2)	2.506(2)	Ca(1)−O(5)	2.582(3)	Ca(1)−O(6)	2.479(3)
Ca(1)−O(3)	2.448(3)	Ca(1)−O(4)	2.548(2)	Ca(1)−O(7)	2.356(3)	Ca(1)−N(1)	2.574(3)
O(1)−Ca(1)−O(2)	93.17(8)	O(1)−Ca(1)−O(3)	94.13(9)	O(3)−Ca(1)−O(7)	114.95(9)	O(3)−Ca(1)−N(1)	130.38(9)
O(1)−Ca(1)−O(4)	86.21(8)	O(1)−Ca(1)−O(5)	149.04(9)	O(4)−Ca(1)−O(5)	64.13(9)	O(4)−Ca(1)−O(6)	124.17(9)
O(1)−Ca(1)−O(6)	144.75(9)	O(1)−Ca(1)−O(7)	90.30(9)	O(4)−Ca(1)−O(7)	80.34(9)	O(4)−Ca(1)−N(1)	158.88(9)
O(1)−Ca(1)−N(1)	79.12(9)	O(2)−Ca(1)−O(3)	64.69(9)	O(5)−Ca(1)−O(6)	60.79(9)	O(5)−Ca(1)−O(7)	76.76(9)
O(2)−Ca(1)−O(4)	129.83(9)	O(2)−Ca(1)−O(5)	112.21(9)	O(5)−Ca(1)−N(1)	126.36(9)	O(6)−Ca(1)−O(7)	79.21(9)
O(2)−Ca(1)−O(6)	80.75(9)	O(3)−Ca(1)−O(7)	149.78(9)	O(6)−Ca(1)−N(1)	66.53(9)	O(7)−Ca(1)−N(1)	84.60(9)
O(2)−Ca(1)−N(1)	66.68(9)	O(3)−Ca(1)−O(4)	65.33(9)	Ca(1)−O(1)−C(1)	132.3(2)		
O(3)−Ca(1)−O(5)	81.87(10)	O(3)−Ca(1)−O(6)	113.73(10)				

[Sr(**L2**$^-$)(H$_2$O)]BPh$_4$

	molecule 1	molecule 2		molecule 1	molecule 2
Sr(1)−O(1)	2.36(1)	2.38(1)	Sr(1)−O(5)	2.63(1)	2.65(1)
Sr(1)−O(2)	2.63(2)	2.70(1)	Sr(1)−O(6)	2.64(1)	2.68(1)
Sr(1)−O(3)	2.55(2)	2.73(1)	Sr(1)−O(7)	2.59(1)	2.61(1)
Sr(1)−O(4)	2.66(2)	2.69(1)	Sr(1)−N(1)	2.76(2)	2.77(1)

	molecule 1	molecule 2		molecule 1	molecule 2
O(1)−Sr(1)−O(2)	96.1(5)	119.8(4)	O(3)−Sr(1)−O(6)	156.3(5)	147.6(5)
O(1)−Sr(1)−O(3)	94.4(5)	127.9(4)	O(3)−Sr(1)−O(7)	82.9(6)	74.5(5)
O(1)−Sr(1)−O(4)	92.9(5)	96.7(5)	O(3)−Sr(1)−N(1)	121.0(6)	122.6(4)
O(1)−Sr(1)−O(5)	101.8(4)	96.2(5)	O(4)−Sr(1)−O(5)	61.5(5)	60.5(5)
O(1)−Sr(1)−O(6)	108.8(4)	84.5(5)	O(4)−Sr(1)−O(6)	122.1(5)	119.9(5)
O(1)−Sr(1)−O(7)	177.1(5)	157.6(5)	O(4)−Sr(1)−O(7)	84.8(5)	95.0(5)
O(1)−Sr(1)−N(1)	73.8(5)	72.3(4)	O(4)−Sr(1)−N(1)	166.7(5)	168.6(5)
O(2)−Sr(1)−O(3)	61.6(6)	59.8(4)	O(5)−Sr(1)−O(6)	61.8(5)	59.7(5)
O(2)−Sr(1)−O(4)	120.7(6)	121.6(5)	O(5)−Sr(1)−O(7)	78.7(5)	73.2(5)
O(2)−Sr(1)−O(5)	161.9(5)	141.8(5)	O(5)−Sr(1)−N(1)	120.0(5)	122.3(5)
O(2)−Sr(1)−O(6)	109.7(5)	108.4(5)	O(6)−Sr(1)−O(7)	74.0(5)	73.2(5)
O(2)−Sr(1)−O(7)	83.5(6)	68.5(4)	O(6)−Sr(1)−N(1)	63.8(5)	62.9(4)
O(2)−Sr(1)−N(1)	62.6(5)	64.2(4)	O(7)−Sr(1)−N(1)	108.5(5)	96.3(5)
O(3)−Sr(1)−O(4)	59.3(6)	61.8(5)	Sr(1)−O(1)-C(1)	139(1)	140(1)
O(3)−Sr(1)−O(5)	119.0(5)	109.1(5)			

[a] Estimated standard deviations are give in parentheses.

axial direction from each other. The bond length between Mg^{2+} and the phenolate oxygen O(1) (1.957 Å) is significantly shorter than that with other neutral oxygen and nitrogen atoms (2.11−2.29 Å), demonstrating the strong interaction between Mg^{2+} and the phenolate. The crown ether ring is almost flat, and Mg^{2+} is located nearly at the center of the pentagonal crown ether ring.

The structure of the Ca^{2+}-complex of **L1**$^-$ ([Ca(**L1**$^-$)(CH$_3$OH)$_2$]BPh$_4$) in Figure 2b is quite different from the structure of the corresponding Mg^{2+}-complex, [Mg(**L1**$^-$)(CH$_3$OH)]BPh$_4$ shown in Figure 2a. In this case, coordination number of the metal center is eight, and the pentagonal plane consists of two oxygen atoms [O(2) and O(3)] and one tertiary amine nitrogen [N(1)] from the crown ether, alcoholic oxygen [O(6)] of the external ligand methanol, and the phenolate oxygen [O(1)]. The calcium ion sitting in the center of the pentagonal plane is coordinated by the remaining oxygen atoms [O(4) and O(5)] of the crown ether from the same side of the plane, and the opposite side of the pentagonal plane is occupied by another methanol molecule [O(7)] (Figure 2b). The bond length between the metal ion and the oxygen atoms of the crown ether ring [O(2)−O(5)] is elongated (2.462−2.607 Å) as compared to the reported value for eight-coordinate Ca^{2+}-complexes (∼2.45 Å).[32] As a result, the crown ether ring is significantly distorted from

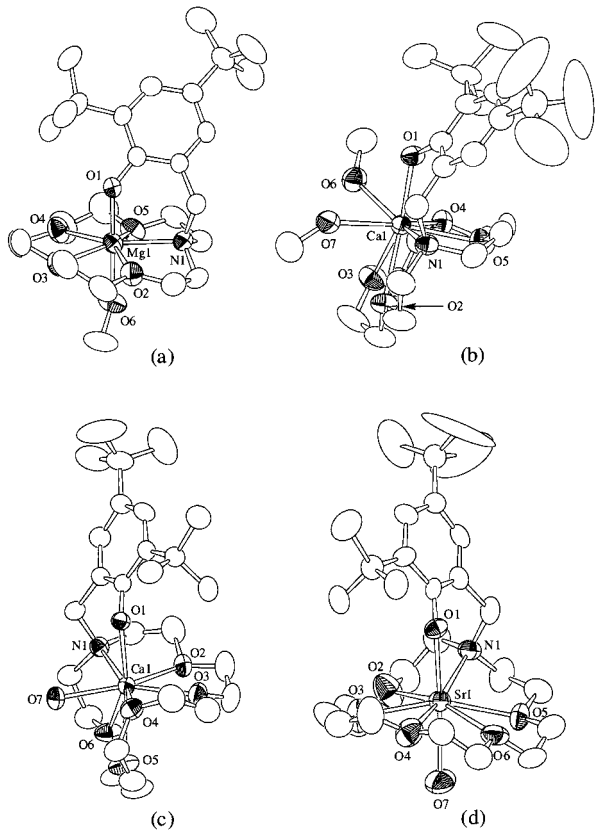

Figure 2. ORTEP drawing of the cationic part of (a) [Mg(**L1**$^-$)(CH$_3$OH)]BPh$_4$, (b) [Ca(**L1**$^-$)(CH$_3$OH)]BPh$_4$, (c) [Ca(**L2**$^-$)(H$_2$O)]BPh$_4$, and (d) [Sr(**L2**$^-$)(H$_2$O)]BPh$_4$. The counteranions and hydrogen atoms are omitted for clarity.

planarity. This kind of structural uniqueness of the Ca^{2+}-complex is not simply attributed to the difference of the metal ion radius as discussed below.

The unique structure of the Ca^{2+}-complex is also seen in the complex of **L2**$^-$. As in the case of **L1**$^-$−complex, the metal center consists of a pentagonal plane with three oxygen atoms [O(4), O(5), and O(6)], one tertiary amine nitrogen atom [N(1)], and the phenolate oxygen [O(1)] of the ligand. One side of the pentagonal plane is also occupied by the remaining oxygen atoms [O(2) and O(3)] of the crown ether ring, whereas the opposite side of the pentagonal plane is filled by the external ligand H_2O [O(7)]. In this case as well, the crown ether ring is bent about 90° along the N(1)−O(4) axis, and the bond length between Ca^{2+} and the oxygen atoms of the crown ether ring [O(2)−O(6)] is elongated (2.448−2.582 Å) as compared to the reported values of eight-coordinated calcium ion (∼2.45 Å).[32] The external ligand H_2O, on the other hand, binds to the metal center fairly strongly (Ca−O(7) = 2.356 Å).

The structure of the Sr^{2+}-complex of **L2**$^-$ looks rather normal, even though the ionic radius of Sr^{2+} (1.12 Å) is larger than that of Ca^{2+} (0.99 Å).[33] The Sr^{2+}-complex has a distorted hexagonal bipyramidal structure in which five neutral oxygen atoms [O(2), O(3), O(4), O(5), and O(6)] and one tertiary amine nitrogen atom [N(1)] from the crown ether ring occupy the basal plane, and the phenolate [O(1)] and water oxygen atoms [O(7)] coordinate to the metal ion center from the opposite axial positions. In this case, Sr^{2+} is placed at nearly the center of the macrocyclic ring of the ligand. Thus, the unique structures of the Ca^{2+}-complexes described above can be attributed to the nature of coordination structure of Ca^{2+}, but to neither the metal ion charge nor the radius. Such a structural uniqueness of Ca^{2+} may be related to its role as signal transduction elements in biological systems, although the origin has yet to be clarified.[34−37]

Table 4. Redox Potentials ($E_{1/2}$ vs SCE/V) of the Phenolate Complexes of **L1**$^-$ and **L2**$^-$ in CH$_3$CN Containing 0.1 M N(^{n}Bu)$_4$PF$_6$

cation	**L1**$^-$	**L2**$^-$
Mg^{2+}	0.59	−
Ca^{2+}	0.41	0.47
Sr^{2+}	0.38	0.36
Ba^{2+}	0.33	0.28
Na^+	0.09	−
K^+	−	0.22
N(^{n}Bu)$_4^+$	−0.14[a]	−0.21[a]

[a] Determined by SHACV.

Change in the Redox Potentials of Phenolates by the Complexation with Metal Ions. The alkaline earth metal complexes of the phenolate derivatives afforded reversible redox couples in the cyclic voltammetric (CV) measurements in CH$_3$CN (see Figure S1), and the $E_{1/2}$ values determined by the CV measurements are summarized in Table 4. The well-defined reversibility in the redox couples shown in Figure S1 demonstrates that the phenoxyl radical−metal complexes are fairly stable at ambient temperature. On the other hand, reversibility in CVs of the phenoxyl radical complexes becomes poor upon going from the divalent metal complexes to the monovalent alkaline metal complexes and totally irreversible voltammograms were obtained in the case of tetra-*n*-butylammonium salts of the phenolate. Thus, the $E_{1/2}$ values of the tetra-*n*-butylammonium salts were determined by the second harmonic ac voltammetry (SHACV) measurements (Figures S2 and S3).[38] The $E_{1/2}$ values of the cation complexes of **L1**$^-$ or **L2**$^-$ in Table 4 increase in order: N(^{n}Bu)$_4^+$ < K^+ (Na^+) < Ba^{2+} < Sr^{2+} < Ca^{2+} < Mg^{2+}. This order agrees with the Lewis acidity of cationic species derived from the superoxide ion complexes with cationic species.[39] Thus, the stronger the Lewis acidity of cationic species, the more positive the $E_{1/2}$ value, that is, the stronger the oxidation ability of the complexes. On the other hand, the effects of the macrocyclic ring size on the redox potential (**L1**$^-$ vs **L2**$^-$) is not so evident.

Characterization of Phenoxyl Radical−Metal Complexes. The one-electron oxidation of [Ca(**L1**$^-$)(CH$_3$OH)$_2$]$^+$ by (NH$_4$)$_2$[Ce^{4+}(NO$_3$)$_6$] (CAN) ($E_{1/2}$ = 1.0 V vs SCE) in CH$_3$CN resulted in a spectral change shown in Figure 3. The absorption band at 309 nm due to the phenolate complex immediately decreases together with a concomitant increase in the new absorption bands at 387, 404, and 682 nm at 25 °C. Similar spectral change

(32) Katz, A. K.; Glusker, J. P.; Beebe, S. A.; Bock, C. W. *J. Am. Chem. Soc.* **1996**, *118*, 5752−5763.

(33) *Handbook of Chemistry and Physics*, 61st ed.; CRC Press: Boca Raton, FL, 1981.

(34) Sigel, H. *Calcium and Its Role in Biology, Metal Ions in Biological Systems*; Marcel Dekker: New York, 1984; Vol. 17.

(35) Spiro, T. G. *Calcium in Biology, Metal Ions in Biology*; Wiley-Interscience: New York, 1983; Vol. 6.

(36) Chazin, W. J. *Nat. Struct. Biol.* **1995**, *2*, 707−710.

(37) Clapham, D. E. *Cell* **1995**, *80*, 259−268.

(38) The SHACV method is known to provide a superior approach to the direct evaluation of the one-electron redox potentials in the presence of a follow-up chemical reaction: (a) McCord, T. G.; Smith, D. E. *Anal. Chem.* **1969**, *41*, 1423−1441. (b) Bond, A. M.; Smith, D. E. *Anal. Chem.* **1974**, *46*, 1946−1951. (c) Wasielewski, M. R.; Breslow, R. *J. Am. Chem. Soc.* **1976**, *98*, 4222−4229. (d) Arnett, E. M.; Amarnath, K.; Harvey, N. G.; Cheng, J.-P. *J. Am. Chem. Soc.* **1990**, *112*, 344−355. (e) Fukuzumi, S.; Fujita, M.; Maruta, J.; Chanon, M. *J. Chem. Soc., Perkin Trans. 2* **1994**, 1597−1602. A well-defined symmetrical SHACV trace was obtained for the one-electron oxidation of the tetra-*n*-butylammonium salts of **L1**$^-$ and **L2**$^-$ in CH$_3$CN as shown in Figure S1 and S2, in which the intersection with the dc potential axis corresponds to the redox potential ($E_{1/2}$).

(39) Fukuzmi, S.; Ohkubo, K. *Chem. Eur. J.* **2000**, *6*, 4532−4535.

Table 5. UV−Vis Data (λ_{Max}/nm and ε/M^{-1} cm^{-1}) of the Phenoxyl Radical Complexes

cation	**L1•**			**L2•**		
Mg^{2+}	393 (2130)	408 (2630)	738 (180)	388 (1370)	406 (1600)	640 (170)
Ca^{2+}	387 (2140)	404 (2580)	682 (230)	388 (2660)	400 (3210)	694 (300)
Sr^{2+} [a]	385	402	672	380	398	668
Ba^{2+} [a]	387	406	627	−	404	626
Na^{+}	388 (1180)	406 (1270)	635 (180)	−	−	−
K^{+}	−	−	−	389 (2200)	407 (2040)	656 (130)
$N(^nBu)_4^{+}$	386 (2700)	406 (2460)	635 (220)	384 (2260)	404 (1880)	645 (170)

[a] Precipitation of $Sr(NO_3)_2$ and $Ba(NO_3)_2$ caused by the CAN oxidation prevented us to determine the accurate value of ε.

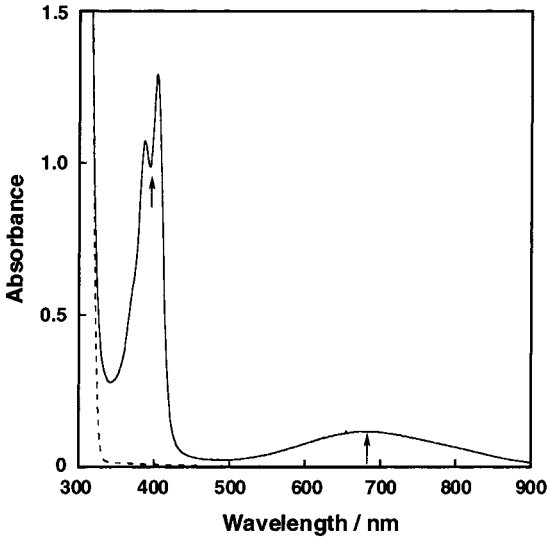

Figure 3. UV−vis spectrum of $[Ca(\mathbf{L1}^{\bullet})(NO_3)]^+$ (solid line) generated by the oxidation of $[Ca(\mathbf{L1}^-)(CH_3OH)]BPh_4$ (dotted line) (5.0×10^{-4} M) by CAN (5.0×10^{-4} M) in CH_3CN at 25 °C.

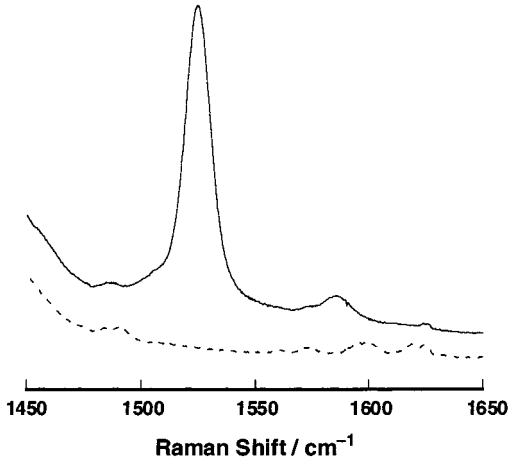

Figure 4. Resonance Raman spectrum of $[Ca(\mathbf{L1}^{\bullet})(NO_3)]^+$ (solid line) (1.5×10^{-3} M) in CH_3CN at −40 °C and that of the same compound decomposed at 25 °C (dotted line).

Table 6. Resonance Raman Data (cm^{-1}) of the Phenoxyl Radical Complexes in CH_3CN at −40 °C

	L1•		**L2•**	
cation	ν_{7a}'	ν_{8a}'	ν_{7a}'	ν_{8a}'
Mg^{2+}	1517	1590	1507	nd[a]
Ca^{2+}	1525	1586	1523	1587
Sr^{2+}	1524	1584	1519	1586
Ba^{2+}	1506	nd	1509	nd
Na^{+}	1506	nd	−	−
K^{+}	−	−	1505	nd

[a] nd: Not detected.

was observed in the oxidation of other phenolate complexes by CAN under the same experimental conditions. The λ_{max} and ε values of the oxidation products are listed in Table 5. All of the spectra exhibit a similar shape having strong absorption bands around 400 nm together with a very broad one in the near-infrared (NIR) region (600−900 nm), which is typical for phenoxyl radical species.[9−16,40] The ZINDO calculation on phenoxyl radical **L1•** [27] suggested that the 400 nm band is mainly associated with a $\pi-\pi^*$ transition (HOMO−1-to-LUMO+1); both molecular orbitals exist on the phenyl ring of the phenoxyl radical species. It is also suggested that the broad band in the NIR region is due to the HOMO−1-to-LUMO transition, where the LUMO orbital exists mainly on the C−O bond of the phenoxyl radical species. Thus, the 400 nm bands are hardly affected by the complex formation, whereas the 600−900 nm bands are significantly altered, depending on the type of metal ions (Table 5). It is interesting to note that the NIR band shifts toward the lower-energy direction with an increase in the Lewis acidity of the metal ion when the $E_{1/2}$ value is shifted to the positive direction (Table 4), although some exceptions are seen in the case of **L2•**. This shows a sharp contrast to the case of the phenolate complexes, where the λ_{max} of the phenolate shifts toward the higher-energy direction with an increase in the Lewis acidity of the metal ion (Table 1). The stronger interaction between the phenoxyl radical oxygen and the metal ion may result in a decrease in the C−O centered LUMO level, thereby leading to a decrease in the HOMO−1-to-LUMO transition energy.

The resonance Raman spectra of the phenoxyl radical−metal complexes excited at 406.7 nm display one prominent peak at 1505−1525 cm^{-1} together with a small one at around 1590 cm^{-1} as listed in Table 6. A typical example of the RR spectrum is shown in Figure 4, and spectra of others are presented as Supporting Information (Figures S4−S12). These bands are vibrational modes characteristic of phenoxyl radicals and are assigned to the modes ν_{7a}' and ν_{8a}' which predominantly consist of the C−O stretching and the $C_{ortho}-C_{meta}$ stretching, respectively.[41] The higher energy of the C−O stretching of the phenoxyl radical (ν_{7a}') as compared to that of a phenolate (ν_{7a} $\approx$ 1250 cm^{-1})[10] clearly indicates that the C−O bond of the phenoxyl radical species has a partial double bond character, and this character is most pronounced in the Ca^{2+}-complexes (Table 6).

The electrospray ionization mass spectrum (ESI-MS) shown in Figure S13 exhibits only a set of prominent peaks with a mass and an isotope distribution pattern being consistent with those of the Ca^{2+}-complexes of the phenoxyl radical species **L1•** and **L2•** with one nitrate ion as a counteranion coming from CAN: $[Ca(\mathbf{L1}^{\bullet})(NO_3)]^+$ and $[Ca(\mathbf{L2}^{\bullet})(NO_3)]^+$. Oxidation of the phenolate complexes of other metal ions also gave similar

(40) Johnston, L. J.; Mathivanan, N.; Negri, F.; Siebrand, W. *Can. J. Chem.* **1993**, *71*, 1655−1662.

(41) Schnepf, R.; Sokolowski, A.; Müller, J.; Bachler, V.; Wieghardt, K.; Hildebrandt, P. *J. Am. Chem. Soc.* **1998**, *120*, 2352−2364.

Table 7. ESR Data of the Phenoxyl Radical Complexes in CH_3CN at −40 °C

	L1•		**L2•**	
cation	g	a_H/G	g	a_H/G
Mg^{2+}	2.0039	6.42	2.0046	6.06
Ca^{2+}	2.0043	6.77	2.0042	6.77
Sr^{2+}	2.0045	7.49	2.0043	6.42
Ba^{2+}	2.0045	6.06	2.0042	6.30
Na^+	2.0046	6.42	−	−
K^+	−	−	2.0045	5.35
$N(^nBu)_4^+$	2.0048	5.88	2.0046	4.17[a]

[a] The a_H value was determined by computer simulation using ESRaII version 1.01 (Calleo Scientific Publisher) on a Macintosh personal computer.

results, confirming the formation of the corresponding phenoxyl radical−metal complexes.

The phenoxyl radical−metal complexes exhibit a doublet ESR signal at $g = 2.0039 \sim 2.0046$ in CH_3CN at −40 °C. The ESR spectra of the phenoxyl radical species are presented as Supporting Information (Figures S14−S25), and their ESR parameters are summarized in Table 7. The hyperfine splitting into a doublet is due to a spin-nucleus coupling with one of the benzylic methylene protons. Coordination of the phenoxyl oxygen to the metal center will inhibit the free rotation around the C(2)−C(2′: benzylic carbon) bond, fixing the steric relation between the benzylic protons and the aromatic ring. As a result, one of the C−H bond is nearly perpendicular to the aromatic plane but another C−H bond is nearly horizontal to the phenoxyl radical ring. Thus, only one methylene proton exhibits the hyperfine coupling.[42,43] Thus, the differences in the hyperfine coupling constants a_H among the phenoxyl radical−metal complexes are largely attributed to the differences in the molecular geometry of the phenoxyl radical complexes as seen in the phenolate complexes discussed above (Figure 2). It should be noted that the g values of the phenoxyl radical complexes decrease upon going from $N(^nBu)_4^+$ to Mg^{2+}. The deviation of g values of the phenoxyl radical complexes from the free spin value ($g_e = 2.0023$) can be expressed in terms of the spin−orbit coupling constant of the oxygen atom (ξ) and the energy gap (δ) between the singly occupied orbital (SOMO) and the nonbonding orbital as given by eq 1.[44] A constant (C) is a value determined by the coefficients of the SOMO and nonbonding orbitals of the phenoxyl radical complexes.[44] The stronger interaction of metal ions with the nonbonding orbital with an increase in the Lewis acidity of metal ion, the larger the energy gap (δ), and thereby the smaller is the g value as observed experimentally.[45]

$$g = g_e + C\xi/\delta \quad (1)$$

Kinetic Stability of the Phenoxyl Radical−Metal Complexes. The phenoxyl radical−metal complexes generated by the CAN oxidation gradually decompose at room temperature.

Scheme 1

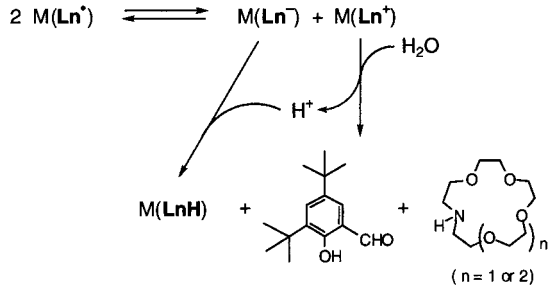

Table 8. Second-order Rate Constants k_{dec} (M^{-1} s^{-1}) for the Decomposition of Phenoxyl Radical Complexes in CH_3CN at 25 °C

cation	**L1•**	**L2•**
Mg^{2+}	108	−
Ca^{2+}	78.6	15.1
Sr^{2+}	134	51.9
Na^+	643	−
$N(^nBu)_4^+$	844	962

The decrease in the absorption band due to the phenoxyl radical complex obeys second-order kinetics, indicating that the decay occurs via a bimolecular disproportionation reaction (see Figure S26). The second-order rate constants (k_{dec}) for the decomposition of the phenoxyl radical complexes were determined from the second-order plots (the inset of Figure S26), and the results are given in Table 8. The mass spectral analysis on the final reaction mixture indicated that *N*-dealkylation products (3,5-di-*tert*-butyl-2-hydroxy-benzaldehyde and the aza-crown ether) were formed together with the original phenol derivative (**LnH**).[27] Thus, the disproportionation reaction between the two phenoxyl radical−metal complexes yields the original phenolate complex [M(**Ln**$^-$)] and the organic cation complex [M(**Ln**$^+$)], the latter of which further decomposes into 3,5-di-*tert*-butyl-2-hydroxy-benzaldehyde and the corresponding crown ether by hydrolysis as shown in Scheme 1. The hydrolysis of organic cation **Ln**$^+$ into the aldehyde derivative and the crown ether will afford one proton (H^+) which may bind to the initially formed phenolate complex [M(**Ln**$^-$)] to provide the phenol derivative (**LnH**).

The k_{dec} values in Table 8 are regarded as measure of the kinetic stability of the phenoxyl radicals, which vary significantly depending on the type of cationic species. The kinetic stabilities of the Ca^{2+}-complexes are most high among the phenoxyl radicals examined (Table 8).[46] Since the disproportionation reaction between the two phenoxyl radicals involves both the oxidation and reduction, the phenoxyl radical species must act as both the oxidant and reductant. The stronger Lewis acid would accelerate the reduction of phenoxyl radical (**Ln•**) to the phenolate (**Ln**$^-$) as indicated by the more positive value of $E_{1/2}$ which corresponds to the reduction potential of **Ln•** (Table 4), but at the same time it would decelerate the oxidation process due to the repulsive interaction between the oxidized product (**Ln**$^+$) and the metal cations. As a result of these contradictory factors, the decomposition (disproportionation) reaction is slowest in the case of a mild Lewis acid such as Ca^{2+}. The kinetic stability of the phenoxyl radical−metal complexes is enhanced in the **L2**−ligand system as compared to the **L1**−ligand system (e.g., compare k_{dec} of Ca^{2+}- and Sr^{2+}-complexes of **L1•** and **L2•**), although the stability of the metal-free radicals is nearly the same. The higher kinetic stability of

(42) Itoh, S.; Taki, M.; Kumei, H.; Takayama, S.; Nagatomo, S.; Kitagawa, T.; Sakurada, N.; Arakawa, R.; Fukuzumi, S. *Inorg. Chem.* **2000**, *39*, 3708−3711.

(43) It has been reported that hyperfine coupling constant (hfc) of phenoxyl radicals can be estimated by the angle-dependent McConnell-type relationship: $a_{C-H} = \rho_{C1}B\cos^2\theta$, where a_{C-H} is the hfc of the methylene proton, ρ_{C1} is the spin density at the C_1 position, B is a constant equal to 162 Hz, and θ is the dihedral angle defined in Figure 8 of Babcock's paper: Babcock, G. T.; El-Deeb, M. K.; Sandusky, P. O.; Whittaker, M. M.; Whittaker, J. W. *J. Am. Chem. Soc.* **1992**, *114*, 3727−3734.

(44) Wertz, J. E.; Bolton, J. R. *Electron Spin Resonance Elementary Theory and Practical Applications*; McGraw-Hill: New York, 1972.

(45) Fukuzumi, S.; Okamoto, T. *J. Am. Chem. Soc.* **1993**, *115*, 11600−11601.

(46) Precipitation of $Ba(NO_3)_2$ caused by the CAN oxidation prevented the kinetic studies of the decomposition process of [Ba(**Ln•**)]$^{2+}$.

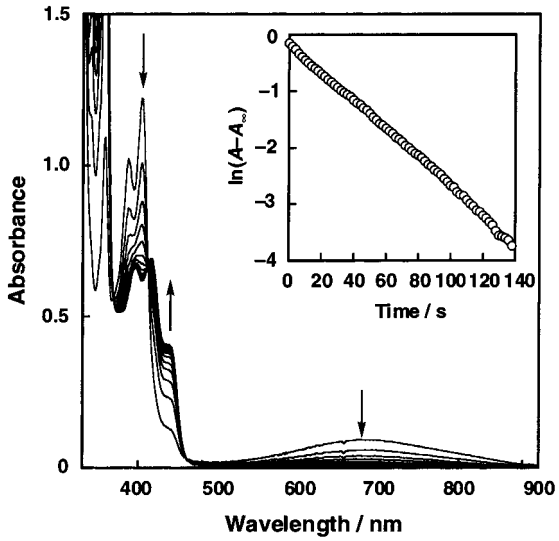

Figure 5. Spectral change for the oxidation of $AcrH_2$ (5.0×10^{-3} M) by $[Ca(\mathbf{L1^{\bullet}})(NO_3)]^+$ (5.0×10^{-4} M) in CH_3CN at −40 °C. Interval: 16 s. Inset: first-order plot based on the absorption change at 404 nm.

Table 9. Second-order Rate Constants $k_2(M^{-1}\ s^{-1})$ for the Oxidation of $AcrH_2$, $AcrD_2$, and AcrHR (R = Me, Et, and Ph) by M(**L1**•) in CH_3CN at −40 °C

M	$AcrH_2$	$AcrD_2$	$(k^H_2/k^D_2)^a$	AcrHMe	AcrHEt	AcrHPh
Mg^{2+}	15	1.2	(12.5)			
Ca^{2+}	7.2	0.86	(8.4)	0.26	0.11	0.048
Sr^{2+}	3.4	0.48	(7.1)			
Na^+	193	40	(4.9)			

[a] Primary kinetic deuterium isotope effect.

L2•−complexes can be attributed to the larger macrocyclic ring of **L2**•, that may protect the phenoxyl radical center more effectively than the smaller crown ether ring in **L1**•. Such a steric effect of the crown ether ring is not expected in the metal-free radicals, since there is no attractive interaction between the phenoxyl radical and the crown ether moiety.

C−H Bond Activation. Reactivity of the phenoxyl radical−metal complexes toward C−H bond activation has been examined in the hydrogen-transfer reaction from 10-methyl-9,10-dihydroacridine ($AcrH_2$) and its 9-substituted derivatives (AcrHR, R = Me, Et, and Ph). The reactions were performed at −40 °C, where the self-decomposition (disproportionation) of the phenoxyl radical complexes was negligibly slow. The spectral change for the reaction of $[Ca(\mathbf{L1^{\bullet}})(NO_3)]^+$ with $AcrH_2$ is shown in Figure 5, in which the characteristic absorption bands due to the phenoxyl radical complex (387, 404, and 682 nm) decreases in the course of the reaction. The final spectrum of the product is identical to that of the authentic sample of $AcrH^+$ (396, 416, and 440 nm). From the absorption intensity at 440 nm ($\epsilon = 2150\ M^{-1}\ cm^{-1}$) is estimated the yield of $AcrH^+$ as 76%.

In contrast to the self-decomposition of the phenoxyl radical−metal complexes (vide supra), the oxidation of $AcrH_2$ obeys first-order kinetics as shown in the inset of Figure 5, where the first-order rate constant (k_{obs}) was determined from the slope of the first-order plot. The rate was first-order with respect to the $AcrH_2$ concentration, and the second-order rate constant (k_2) was obtained from the slope of a linear plot of k_{obs} versus $[AcrH_2]$. The k_2 values for the oxidation of $AcrH_2$ as well as 9,9-dideuterated derivative ($AcrD_2$) and 9-substituted derivatives (AcrHR) by the series of **L1**• complexes are listed in Table 9. The overall reaction consists of a formal hydrogen atom transfer from AcrHR to M(**Ln**•) to afford AcrR• (R = H, D, Me, Et, or Ph)) and M(**LnH**) and a subsequent electron transfer from the resulting AcrR• to another M(**Ln**•), generating $AcrR^+$ and M(**Ln**$^-$) (Scheme 2). A relatively large primary kinetic isotope effects $k^H_2/k^D_2 = 4.9-12.5$ were obtained when $AcrD_2$ was employed instead of $AcrH_2$, confirming that the initial hydrogen atom transfer is the rate-determining step. Thus, the k_2 values can be regarded as a measure of H•-abstraction ability of the phenoxyl radical−metal complexes.

Scheme 2

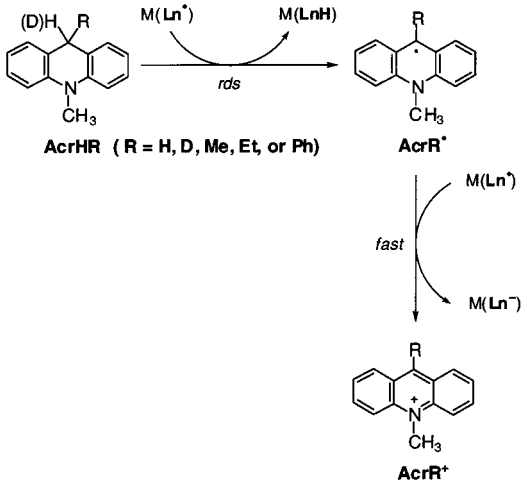

There are two possibilities in the mechanisms of hydrogen-transfer reactions of NADH analogues ($AcrH_2$) to an organic radical oxidant, that is, a one-step hydrogen transfer or electron transfer followed by proton transfer.[29a,47] A one-step (direct) hydrogen transfer from $AcrH_2$ to the phenoxyl radicals would be retarded by the binding of metal ions to the phenoxyl radicals to which the hydrogen atom is to be bound. The reaction rate for the tetra-*n*-butylammonium salt was too fast to be determined accurately, and the Na^+-complex shows significantly higher reactivity than the alkaline earth metal complexes (Table 9). In the case of alkaline earth metal complexes, however, the k_2 value increases in order: $Sr^{2+} < Ca^{2+} < Mg^{2+}$ with increasing the Lewis acidity of metal ions, when the binding of metal ions to the phenoxyl radical becomes stronger. In addition, the k^H_2/k^D_2 value *increases* with increasing the binding strength of metal ions to the phenoxyl radical in order: $Na^+ < Sr^{2+} < Ca^{2+} < Mg^{2+}$. This is completely opposite from what is expected for a one-step hydrogen transfer reaction in which the primary kinetic deuterium isotope effects (k^H_2/k^D_2) should decrease with increasing the binding strength of metal ions to the phenoxyl radical when the driving force of hydrogen transfer decreases.[48] Thus, an alternative mechanism, that is, electron transfer followed by proton transfer shown in Scheme 3 should be considered to account for the reactivity of the alkaline earth metal complexes of phenoxyl radicals and the primary kinetic deuterium isotope effects in Table 9.

Judging from the one-electron oxidation potential of $AcrH_2$ (E^0_{ox} vs SCE = 0.81 V)[49] which is higher than the one-electron reduction potentials of the phenoxyl radical−metal complexes (equivalent to the one-electron oxidation potentials of the phenolate complexes in Table 4), the free energy change of electron transfer from $AcrH_2$ to the phenoxyl radical complexes

(47) Fukuzumi, S.; Tokuda, Y.; Chiba, Y.; Greci, L.; Carloni, P.; Damiani, E. *J. Chem. Soc., Chem. Commun.* **1993**, 1575−1577.

(48) (a) Pryor, W. A.; Kneipp, K. G. *J. Am. Chem. Soc.* **1971**, *93*, 5584−5585. (b) Ishikawa, M.; Fukuzumi, S. *J. Chem. Soc., Faraday Trans.* **1990**, *86*, 3531−3536.

(49) Fukuzumi, S.; Tokuda, Y.; Kitano, T.; Okamoto, T.; Otera, J. *J. Am. Chem. Soc.* **1993**, *115*, 8960−8968.

Scheme 3

$$\mathrm{AcrHR + M(Ln^{\bullet})} \underset{ET}{\rightleftharpoons} \mathrm{[AcrHR^{\bullet+}\ M(Ln^{-})]} \xrightarrow[rds]{} \mathrm{AcrR^{\bullet} + M(LnH)}$$

is positive [ΔG^0_{et} (in eV) = $e(E^0_{ox} - E^0_{red}) > 0$, e is the elementary charge], and thereby the electron-transfer step is endergonic. In such a case, the overall rate of hydrogen transfer (k_2) which consists of electron-transfer and proton-transfer steps would be slower than the initial electron-transfer rate (k_{et}). The maximum k_{et} value is evaluated from the ΔG^0_{et} value by eq 2, where Z is the frequency factor taken as 1×10^{11} M^{-1} s^{-1}, and k_B is the Boltzmann constant.

$$k_{et} = Z \exp(-\Delta G^0_{et}/k_B T) \qquad (2)$$

Figure 6 shows a plot of log k_2 versus ΔG^0_{et} in reference to a linear correlation log k_{et} versus ΔG^0_{et}, calculated by eq 2 (denoted by ET line). The k_2 value of the Na^+−**L1**$^{\bullet}$ complex is significantly above the ET line, whereas those of the alkaline earth metal−**L1**$^{\bullet}$ complexes are much lower than the ET line. The k_2 value of the Na^+−**L1**$^{\bullet}$ complex, which is much larger than the corresponding k_{et} value, indicates that the hydrogen transfer proceeds via a direct one-step hydrogen transfer rather than via electron transfer. In such a case, the primary kinetic deuterium isotope effect is ascribed to the direct transfer of hydrogen atom from $AcrH_2$ to the Na^+−**L1**$^{\bullet}$ complex. The k^H_2/k^D_2 value (4.9) agrees with the value (4.8) reported for the hydrogen atom transfer from $AcrH_2$ to hydrogen peroxyl radical.[50] On the other hand, the k_2 values of alkaline earth metal−**L1**$^{\bullet}$ complexes, which are much smaller than the corresponding maximum k_{et} values, indicate that the hydrogen transfer proceeds via electron transfer followed by proton transfer as shown in Scheme 3 rather than a direct one-step hydrogen transfer. In such a case, the primary kinetic deuterium isotope effect is ascribed to proton transfer from $AcrH_2^{\bullet+}$ to the alkaline earth metal−**L1**$^{-}$ complexes. The large primary kinetic isotope effects (7.1−12.5) observed for alkaline earth metal−**L1**$^{\bullet}$ complexes (Table 9) are consistent with those reported for proton transfer from $AcrH_2^{\bullet+}$ to semiquinone radical anions (7.2−10.4).[48b]

The diminished reactivity of $AcrH_2$ toward the hydrogen-transfer reaction with the Ca^{2+}−**L1**$^{\bullet}$ complex when $AcrH_2$ is replaced by AcrHR (R = Me, Et, and Ph) shown in Table 9 is also consistent with the electron-transfer−proton-transfer mechanism in Scheme 3, since such diminished reactivity of $AcrH_2$ is also observed for a hydride transfer reaction from AcrHR to tetracyanoethylene (TCNE), which has been shown to proceed via electron transfer from AcrHR to TCNE followed by proton transfer from $AcrHR^{\bullet+}$ to $TCNE^{\bullet-}$.[51] The k_2 values of hydrogen-transfer reactions from AcrHR to the Ca^{2+}−**L1**$^{\bullet}$ complex are compared with the k_h values (k_h: the rate constant of hydride transfer from AcrHR to TCNE)[51] in the logarithmic plots in Figure 7, where the k_2 values are in parallel with the k_h values. Such a parallel relationship confirms the validity of the electron-transfer−proton-transfer mechanism shown in Scheme 3.

The coupling of electron transfer and proton transfer is a well-established alternative for the formal hydrogen atom transfer in many organic reactions.[49] Such a proton-coupled electron transfer has been suggested to play an important role in biological electron transfer.[52] It is often difficult to determine whether the proton-coupled electron transfer is consecutive, that is, electron transfer followed by proton transfer or vice versa, or a concerted process in one quantum mechanical tunneling event.[53] The present study demonstrated for the first time clearly that the hydrogen atom abstraction by the phenoxyl radical−alkaline earth metal complexes proceeds via electron transfer followed by rate-determining proton transfer, providing valuable insight into the C−H bond activation mechanism by tyrosine radicals in biological systems.

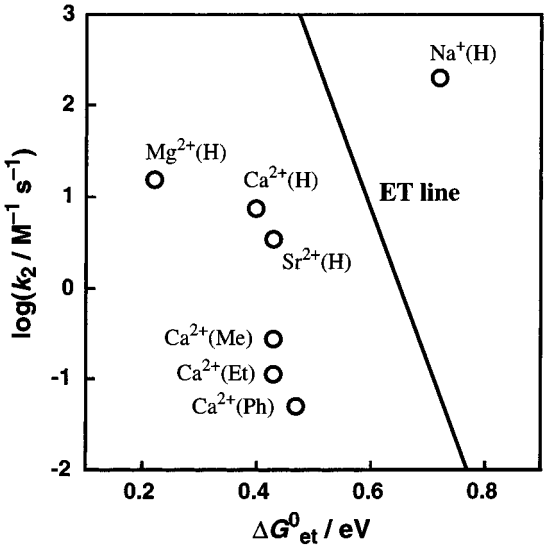

Figure 6. Plot of the rate constant of hydrogen transfer from AcrHR (R = H, Me, Et, and Ph) to the phenoxyl radical complexes M(**L1**$^{\bullet}$) (log k_2) vs the free energy of electron transfer from AcrHR to the phenoxyl radical complexes (ΔG^0_{et}). The solid line shows the dependence of the calculated rate constant of electron transfer (k_{et}) on ΔG^0_{et} based on eq 2, see text.

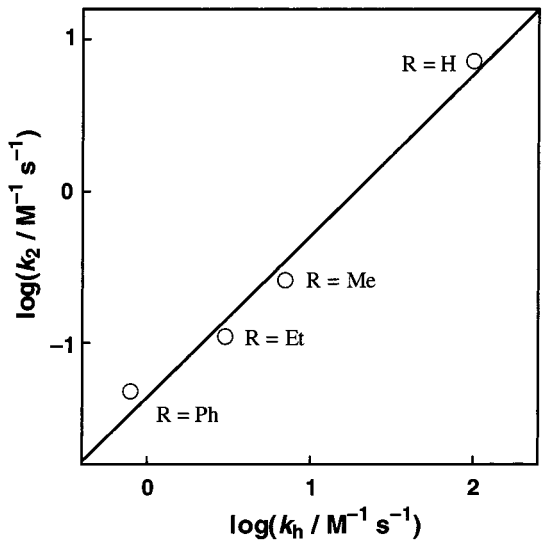

Figure 7. Comparison of the rate constant (log k_2) of hydrogen transfer from AcrHR (R = H, Me, Et, and Ph) to Ca^{2+}(**L1**$^{\bullet}$) and the rate constant (log k_h) of hydride transfer from AcrHR to TCNE (the data were taken from ref 51).

(50) Fukuzumi, S.; Ishikawa, M.; Tanaka, T. *J. Chem. Soc., Perkin Trans. 2* **1989**, 1037−1045.

(51) Fukuzumi, S.; Ohkubo, K.; Tokuda, Y.; Suenobu, T. *J. Am. Chem. Soc.* **2000**, 122, 4286−4294.

(52) (a) Okamura, M. Y.; Feher, G. *Annu. Rev. Biochem.* **1992**, *61*, 861. (b) Malmström, B. G. *Acc. Chem. Res.* **1993**, *26*, 332−338. (c) Ferguson-Miller, S.; Babcock, G. T. *Chem. Rev.* **1996**, *96*, 2889−2907. (d) Hoganson, C. W.; Babcock, G. T. *Science* **1997**, *277*, 1953−1956. (e) Cukier, R. I.; Nocera, D. G. *Annu. Rev. Phys. Chem.* **1998**, *49*, 337−369.

(53) Cukier, R. I. *J. Phys. Chem. A* **1999**, *103*, 5989−5995.

Experimental Section

General. Reagents and solvents used in this study were commercial products of the highest available purity and were further purified by the standard methods.[54] 10-Methyl-9,10-dihydroacridine ($AcrH_2$) and its 9,9-dideuterated derivative ($AcrD_2$) were prepared by the reported procedures,[49] and 9-substituted derivatives of $AcrH_2$ (AcrHR, R = Me, Et, and Ph) were obtained from the previous study.[51] IR spectra were recorded on a Shimadzu FTIR-8200PC and UV−vis spectra on a Hewlett-Packard 8453 photodiode array spectrophotometer. ^{1}H NMR spectra were recorded on a JEOL FT-NMR GX-400 spectrometer. ESR spectra were recorded on a JEOL JES-ME-2X spectrometer. The g values were determined using a Mn^{2+} marker as a reference. Mass spectra were recorded on a JEOL JNX-DX303 HF mass spectrometer or a Shimadzu GCMS-QP2000 gas chromatograph mass spectrometer. ESI-MS (electrospray ionization mass spectra) measurements were performed on a JEOL JMS-700T Tandem Mstation or a PE SCIEX API 150EX. Molecular orbital calculations were performed by using a CAChe program (Version 3.2). The UV−visible electronic transitions are calculated with ZINDO using INDO/1 parameters after optimizing geometry with Augmented MM3 and MOPAC PM3. The cyclic voltammetry measurements were performed on a BAS 100 W or a ALS 600 electrochemical analyzer in deaerated CH_3CN containing 0.10 M NBu_4PF_6 as supporting electrolyte. The Pt and Au working electrodes (BAS) were polished with BAS polishing alumina suspension and rinsed with acetone before use. The counter electrode was a platinum wire. The measured potentials were recorded with respect to an $Ag/AgNO_3$ (0.01 M) reference electrode. The $E_{1/2}$ values (vs $Ag/AgNO_3$) are converted to those vs SCE by adding 0.29 V.[55] All electrochemical measurements were carried out at 25 °C under an atmospheric pressure of nitrogen.

Resonance Raman Measurement. The 406.7 nm line of a Kr^+ laser (model 2060 Spectra Physics) was used as the exciting source. Visible resonance Raman scattering was detected with a liquid nitrogen cooled CCD detector (model LN/CCD-1340 × 400PB, Princeton Instruments) attached to a 1 m single polychlomator (model MC-100DG, Ritsu Oyo Kogaku). The slit width and slit height were set to be 200 μm and 20 mm, respectively. Wavenumber width per channel is 0.35 cm^{-1}, which determines the wavenumber resolution in this measurement. The laser power used was 8.9 mW at the sample point. All measurements were carried out at −40 °C with a spinning cell (1000 rpm). Raman shifts were calibrated with indene, and accuracy of the peak positions of the Raman bands was ±1 cm^{-1}.

X-ray Structure Determination. Data of X-ray diffraction were collected by Rigaku RAXIS-RAPID imaging plate two-dimensional area detector using graphite-monochromated MoKα radiation (λ = 0.71070 Å) to 2θ max of 55.0 °. The intensity measurement was undertaken by sealing them in a glass capillary tube containing the mother liquid. All of the crystallographic calculations were performed by using teXsan software package of the Molecular Structure Corporation [teXsan: Crystal Structure Analysis Package, Molecular Structure Corp. (1985 and 1999)]. The crystal structure was solved by the direct methods and refined by the full-matrix least squares. All non-hydrogen atoms and hydrogen atoms were refined anisotropically and isotropically. The summary of the fundamental crystal data and experimental parameters for structure determinations is given in Table 2. The experimental details including data collection, data reduction, and structure solution and refinement as well as the atomic coordinates and B_{iso}/B_{eq}, anisotropic displacement parameters, and intramolecular bond distances and angles have been deposited in the Supporting Information (S23−S26).

Syntheses. 2,4-Di-*tert*-butyl-6-(1,4,7,10-tetraoxa-13-aza-cyclopentadec-13-ylmethyl)-phenol (L1H). A mixture of 1-aza-15-crown-5 (1 mmol, 219.3 mg), paraformaldehyde (2 mmol, 60.0 mg), and 2,4-di-*tert*-buthylphenol (2 mmol, 412.7 mg) in ethanol (10 mL) was refluxed for 1 day. Removal of the solvent gave an oily material from which **L1H** was isolated by column chromatography (SiO_2, $CHCl_3$) in 80% yield (348.8 mg): IR (neat) 3000 (hydrogen bonding phenolic OH), 1361, 1241, and 1129 cm^{-1} (O−H, C−O); ^{1}H NMR (400 MHz, $CDCl_3$) δ 1.29 (s, 9H), 1.44 (s, 9H), 2.86 (t, J = 5.9 Hz, 4H), 3.63−3.61 (m, 4H), 3.67 (t, J = 5.9 Hz, 4H), 3.69 (s, 4H), 3.72−3.70 (m, 4H), 3.80 (s, 2H), 6.84 (d, J = 2.2 Hz, 1H), 7.21 (d, J = 2.2 Hz, 1H); HRMS m/z 437.3152, calcd for $C_{25}H_{43}NO_5$ 437.3141; UV−vis (CH_3CN) λ_{max} = 284 nm (ϵ = 2250 M^{-1} cm^{-1}).

2,4-Di-*tert*-butyl-6-(1,4,7,10,13-pentaoxa-16-aza-cyclooctadec-16-ylmethyl)-phenol (L2H). This compound was prepared using 1-aza-18-crown-6 in place of 1-aza-15-crown-5 by a similar procedure for the synthesis of **L1H** in 83% yield: IR (neat) 3000 (hydrogen bonding phenolic OH), 1360, 1241, and 1123 cm^{-1} (O−H, C−O); ^{1}H NMR (400 MHz, $CDCl_3$) δ 1.27 (s, 9H), 1.41 (s, 9H), 2.84 (t, J = 5.5 Hz, 4H), 3.61−372 (m, 20H), 3.80 (s, 2H), 6.82 (d, J = 2.2 Hz, 1H), 7.19 (d, J = 2.2 Hz, 1H); HRMS m/z 481.3409, calcd for $C_{27}H_{47}NO_6$ 481.3403; UV−vis (CH_3CN) λ_{max} = 283 nm (ϵ = 2360 M^{-1} cm^{-1}).

[Na(L1$^-$)]. NaH in oil (70 wt %) (0.4 mmol, 13.7 mg) was washed with dry *n*-hexane three times to remove the oily material before the reaction. Then, a dry THF solution (5 mL) of **L1H** (0.4 mmol, 175 mg) was added to NaH slowly. The mixture was stirred for several minutes at room temperature. After removal of insoluble material by filtration, addition of *n*-hexane (30 mL) to the filtrate gave colorless micro crystal in 55% yield: UV−vis (CH_3CN) λ_{max} = 320 nm (ϵ = 5520 M^{-1} cm^{-1}); FAB-MS m/z 460 (Na(**L1**$^-$) + H^+). Anal. Calcd for [Na(**L1**$^-$)], $C_{25}H_{42}NO_5Na$: C, 65.33; H, 9.21; N, 3.05. Found: C, 65.07; H, 9.16; N, 3.05.

[K(L2$^-$)]. This complex was prepared in a grove box ([O_2] < 1 ppm, [H_2O] < 1 ppm) as follows. KH in oil (35 wt %) (0.4 mmol, 45.8 mg) was washed with dry *n*-hexane three times to remove the oily material before the reaction. Then, a dry THF solution (5 mL) of **L1H** (0.4 mmol, 192.6 mg) was added to KH slowly. The mixture was stirred for several minutes at room temperature. After removal of the solvent, the resulting material was washed with dry *n*-hexane to afford white solid in 25% yield: UV−vis (CH_3CN) λ_{max} = 312 nm (ϵ = 3100 M^{-1} cm^{-1}); FAB-MS m/z 520 (K(**L2**$^-$) + H^+). Anal. Calcd for for [K(**L2**$^-$)]·$2H_2O$, $C_{27}H_{50}NO_7K$: C, 58.34; H, 9.07; N, 2.52. Found: C, 58.95; H, 8.57; N, 2.48.

[Mg(L1$^-$)(CH_3OH)]BPh_4. To a mixture of **L1H** (0.2 mmol, 87.5 mg) and triethylamine (0.2 mmol, 28.7 μL) in methanol (5 mL) was added $Mg(ClO_4)_2$ (0.2 mmol, 44.6 mg) in methanol (5 mL) dropwise with stirring at ambient temperature. Addition of $NaBPh_4$ (0.4 mmol, 136.9 mg) in methanol (5 mL) to the mixture gave colorless micro crystals, which were recrystallized from methanol to give pure material of the Mg^{2+}-complex in 61% yield: UV−vis (CH_3CN) λ_{max} = 304 nm (ϵ = 4000 M^{-1} cm^{-1}); FAB-MS m/z 460 (Mg(**L1**$^-$)$^+$). Anal. Calcd for [Mg(**L1**$^-$)(CH_3OH)]BPh_4, $C_{50}H_{66}NO_6BMg$: C, 73.93; H, 8.19; N, 1.72. Found: C, 73.86; H, 8.29; N, 1.70.

[Ca(L1$^-$)(CH_3OH)$_2$]BPh_4. This complex was prepared in a similar manner for the synthesis of [Mg(**L1**$^-$)(CH_3OH)]BPh_4 by using $Ca(ClO_4)_2$·$4H_2O$ (0.2 mmol, 62.2 mg) instead of $Mg(ClO_4)_2$ (91% yield): UV−vis (CH_3CN) λ_{max} = 309 nm (ϵ = 3940 M^{-1} cm^{-1}); FAB-MS m/z 476 (Ca(**L1**$^-$)$^+$). Anal. Calcd for [Ca(**L1**$^-$)(CH_3OH)$_2$]BPh_4, $C_{51}H_{70}NO_7BCa$: C, 71.22; H, 8.20; N, 1.63. Found: C, 71.36; H, 7.91; N, 1.82.

[Sr(L1$^-$)(CH_3OH)$_2$]BPh_4. This complex was prepared in a similar manner for the synthesis of [Mg(**L1**$^-$)(CH_3OH)]BPh_4 by using $Sr(ClO_4)_2$ (0.2 mmol, 57.3 mg) instead of $Mg(ClO_4)_2$ (84% yield): UV−vis (CH_3CN) λ_{max} = 310 nm (ϵ = 4160 M^{-1} cm^{-1}); FAB-MS m/z 524 (Sr(**L1**$^-$)$^+$). Anal. Calcd for [Sr(**L1**$^-$)(CH_3OH)$_2$]BPh_4, $C_{51}H_{70}NO_7BSr$: C, 67.49; H, 7.77; N, 1.54. Found: C, 66.98; H, 7.44; N, 1.68.

[Ba(L1$^-$)(CH_3OH)$_2$]BPh_4. This complex was prepared in a similar manner for the synthesis of [Mg(**L1**$^-$)(CH_3OH)]BPh_4 by using $Ba(ClO_4)_2$·$3H_2O$ (0.2 mmol, 78.1 mg) instead of $Mg(ClO_4)_2$ (88% yield): UV−vis (CH_3CN) λ_{max} = 311 nm (ϵ = 3460 M^{-1} cm^{-1}); FAB-MS m/z 574 (Ba(**L1**$^-$)$^+$). Anal. Calcd for [Ba(**L1**$^-$)(CH_3OH)$_2$]BPh_4, $C_{51}H_{70}NO_7BBa$: C, 63.99; H, 7.37; N, 1.46. Found: C, 63.76; H, 7.07; N, 1.67.

[Ca(L2$^-$)(H_2O)]BPh_4. This complex was prepared in a similar manner for the synthesis of [Ca(**L1**$^-$)(CH_3OH)]BPh_4 70% yield: UV−vis (CH_3CN) λ_{max} = 306 nm (ϵ = 4820 M^{-1} cm^{-1}); FAB-MS m/z 520

(54) Perrin, D. D.; Armarego, W. L. F. *Purification of Laboratory Chemicals*; Butterworth-Heinemann: Oxford, 1988.

(55) Mann, K.; Barnes, K. K. *Electrochemical Reactions in Nonaqueous Systems*; Marcel Dekker Inc.: New York, 1990.

($Ca(\mathbf{L2}^-)^+$). Anal. Calcd for $[Ca(\mathbf{L2}^-)(H_2O)]BPh_4$, $C_{51}H_{68}NO_7BCa$: C, 71.39; H, 7.99; N, 1.63. Found: C, 71.24; H, 7.89; N, 1.69.

$[Sr(\mathbf{L2}^-)(H_2O)]BPh_4 \cdot 0.5CH_3OH$. This complex was prepared in a similar manner for the synthesis of $[Sr(\mathbf{L1}^-)(CH_3OH)_2]BPh_4$ 60% yield: UV−vis (CH_3CN) $\lambda_{max} = 308$ nm ($\epsilon = 4840\ M^{-1}\ cm^{-1}$); FAB-MS *m*/*z* 568 ($Sr(\mathbf{L2}^-)^+$). Anal. Calcd for $[Sr(\mathbf{L2}^-)(H_2O)]BPh_4 \cdot 0.5CH_3OH$, $C_{51.5}H_{70}NO_{7.5}BSr$: C, 67.12; H, 7.66; N, 1.52. Found: C, 66.87; H, 7.30; N, 1.24.

$[Ba(\mathbf{L2}^-)(H_2O)](BPh_4) \cdot 0.5CH_3OH$. This complex was prepared in a similar manner for the synthesis of $[Ba(\mathbf{L1}^-)(CH_3OH)_2]BPh_4$ 89% yield: UV−vis (CH_3CN) $\lambda_{max} = 310$ nm ($\epsilon = 3560\ M^{-1}\ cm^{-1}$); FAB-MS *m*/*z* 618 ($Ba(\mathbf{L2}^-)^+$). Anal. Calcd for $[Ba(\mathbf{L2}^-)(H_2O)]BPh_4 \cdot 0.5CH_3OH$, $C_{51.5}H_{70}NO_{7.5}BBa$: C, 63.69; H, 7.26; N, 1.44. Found: C, 63.54; H, 6.99; N, 1.54.

Kinetics. The phenoxyl radical species of the alkaline and alkaline earth metal complexes were generated in situ by adding an equimolar amount of $(NH_4)_2[Ce^{4+}(NO_3)_6]$ (CAN, 5.0×10^{-4} M) into a deaerated CH_3CN solution of the corresponding phenolate complex (5.0×10^{-4} M) in a UV cell (1 cm path length, sealed tightly with a silicon rubber cap) at 25 °C. The rate constants for the self-decomposition reaction (k_{dec}) of the phenoxyl radical complexes were determined by following a decrease in the absorption band due to the phenoxyl radical.

The oxidation of $AcrH_2$ and AcrHR by the phenoxyl radical species was initiated by adding the substrate into the CH_3CN solution, when the absorption of the phenoxyl radical complexes reached a maximum in a few minutes after the addition of CAN into the phenolate complex solution at −40 °C. The rate constants (k_{obs}) for the redox reactions were also determined by following a decrease in the absorption due to the phenoxylradical species.

Acknowledgment. This work was partially supported by Grants-in-Aid for Scientific Research Priority Area (Nos. 11228205, 11228206) and Grants-in-Aid for Scientific Research (Nos. 11440197 and 12874082) from the Ministry of Education, Science, Culture and Sports, Japan.We also thank Professor Yasushi Kai and co-workers, especially Dr. Nobuko Kanehisa, of Osaka University for their assistance in the X-ray measurements and Professor Hiroshi Tsukube of Osaka City University for his helpful discussion.

Supporting Information Available: The cyclic voltammogram of $[Ca(\mathbf{L1}^-)(CH_3OH)]BPh_4$ (Figure S1), the SHACVs of tetra-*n*-butylammonium salts of $\mathbf{L1}^-$ and $\mathbf{L2}^-$ (Figures S2 and S3), resonance Raman spectra of the phenoxyl radical species (Figures S4−S12), ESI-MS of $[Ca(\mathbf{L1}^{\bullet})(NO_3)]^+$ and $[Ca(\mathbf{L2}^{\bullet})(NO_3)]^+$ (Figure S13), ESR spectra (Figures S14−S25) of the phenoxyl radical complexes, spectral change for the decomposition of $[Ca(\mathbf{L1}^{\bullet})(NO_3)]^+$ (Figure S26), and details about the X-ray structure determination including crystallographic data (S27−S30) (PDF). An X-ray crystallographic file (CIF). This material is available free of charge via the Internet at http://pubs.acs.org.

JA0036110